 MCB, vol.9, no.3, pp.213-226, 2012

Dynamic Lung Modeling and Tumor Tracking Using Deformable Image Registration and Geometric Smoothing

Yongjie Zhang*, Yiming Jing*, Xinghua Liang*, Guoliang Xu†, Lei Dong‡

Abstract: A greyscale-based fully automatic deformable image registration algorithm, based on an optical flow method together with geometric smoothing, is developed for dynamic lung modeling and tumor tracking. In our computational processing pipeline, the input data is a set of 4D CT images with 10 phases. The triangle mesh of the lung model is directly extracted from the more stable exhale phase (Phase 5). In addition, we represent the lung surface model in 3D volumetric format by applying a signed distance function and then generate tetrahedral meshes. Our registration algorithm works for both triangle and tetrahedral meshes. In CT images, the intensity value reflects the local tissue density. For each grid point, we calculate the displacement from the static image (Phase 5) to match with the moving image (other phases) by using merely intensity values of the CT images. The optical flow computation is followed by a regularization of the deformation field using geometric smoothing. Lung volume change and the maximum lung tissue movement are used to evaluate the accuracy of the application. Our testing results suggest that the application of deformable registration algorithm is an effective way for delineating and tracking tumor motion in image-guided radiotherapy.

Keywords: Dynamic lung modeling, tumor tracking, deformable image registration, optical flow, geometric smoothing.

1 Introduction

Today, cancer is the second most common cause of death in the United States. In 2011, about 571,950 Americans are expected to die of cancer. It is estimated

* Department of Mechanical Engineering, Carnegie Mellon University, Pittsburgh, PA 15213, USA. Email: {jessicaz, yjing, xliang1}@andrew.cmu.edu

† LSEC, Institute of Computational Mathematics, Academy of Mathematics and System Sciences, Chinese Academy of Sciences, Beijing 100190, China. Email: xuguo@lsec.cc.ac.cn

‡ Scripps Proton Therapy Center, 9577 Summers Ridge Road, San Diego, CA 92121, USA. Email: Dong.Lei@ScrippsHealth.Org

that 221,130 people will be diagnosed with lung and bronchus cancer, and approximately 156,940 of them will die from this disease [1]. Approximately 45,000-50,000 of these patients will be diagnosed with locally advanced non-small-cell lung cancer (NSCLC) with an expected 5-year survival of only 10-20%. The poor results of radiotherapy for medically inoperable NSCLC may be due to various deficiencies in conventional radiation treatment techniques. One of such deficiencies is the respiratory-induced organ motion, which limits further reduction in treatment margins, and consequently also limits further dose escalation without significantly increasing treatment-related toxicities. There have been numerous studies demonstrating significant respiration motions and their dosimetric effects. However, it was not until recently that 4D CT scans became available. 4D CT images allow for quantitative modeling of internal organ motion for both treatment targets (primary tumors and involved lymph nodes) and normal tissues and organs that may be at risk due to radiation related toxicity. The internal organ motion determined from 4D CT provides evidence-based strategies to improve treatment plans. In addition, CT imaging modality provides the necessary tissue density information needed for radiation transport calculations, which are critical in designing accurate radiation treatments taking into account of density variations due to breathing. However, quantitative dosimetric studies using 4D CT are scarce at the present time. One reason was the need for deformable image registration to track dose deposited in the same target volume in multiple CT images at different time. This technique is still under intense research and development.

As reviewed in [2], four main deformable registration techniques were developed for medical image data: elastic registration, level-set method, diffusion-based registration, and optical flow method. In elastic registration [3]; [4], external forces are introduced to stretch the image while internal forces defined by stiffness or smoothness constraints are applied to minimize the amount of bending and stretching. One of its advantages is that the feature matching and mapping function design can be done simultaneously. The level-set method [5] is a numerical technique for tracking interfaces and shapes, which can easily track topology change and combine segmentation together with registration [6]; [7]. The diffusion-based registration [8]; [9] considers the contours and other features in one image as membranes, and the other image as a deformable grid model, with geometrical constraints. This approach relies mainly on the notion of polarity, as well as the notion of distance. The optical flow method [10]; [11] assumes that the corresponding intensity value in the static image and the moving image stays the same, and then estimates the motion as an image velocity or displacement. This method is suitable for deformations in temporal sequences of images. Optical flow and diffusion registrations can be combined to have better matching results.

In this paper, we develop a systematic computational framework for dynamic lung modeling and tumor tracking using an optical flow registration together with geometric modeling techniques. In our computational processing pipeline, the input data is a set of 4D CT images with 10 phases. The triangle mesh of the lung model is directly extracted from one stable phase (Phase 5). In addition, we represent the lung surface model in 3D volumetric format by applying a signed distance function and then generate tetrahedral meshes. Our registration algorithm works for both triangle and tetrahedral meshes. In CT images, the intensity value reflects the local material density. For each grid point, we calculate the displacement from the Phase 5 image to match with images at other phases by using merely intensity values. The optical flow computation is followed by a regularization of the deformation field using geometric smoothing. Lung volume change and the maximum lung tissue movement are used to evaluate the accuracy of the application. Our testing results suggest that the application of the deformable image registration is an effective way for delineating and tracking tumor motion for image-guided radiotherapy.

The remainder of this paper is organized as follows. Section 2 overviews the systematic computational framework and then the following sections explain details. Section 3 describes an optical flow approach together with geometric smoothing. Section 4 shows testing results, and finally Section 5 draws conclusions.

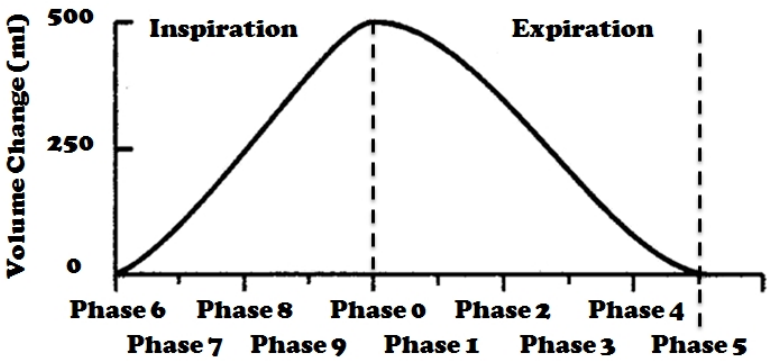

Figure 1: Ten phases during respiration.

2 Computational Framework

The respiration process can be divided into ten phases (Fig. 1), and the CT image data at each phase were obtained automatically from a 4D CT machine. During respiration, the motion of the lung results in the movement of the tumor inside the lung. It is important to study the movement of the lung and find out the exact posi-

tion of the tumor at each phase of respiration. The ultimate goal is to use the lung and tumor tracking results for dose calculation and non-active lung tissue identification during the lung cancer treatment planning. Fig. 2 shows a computational framework of dynamic lung modeling and tumor motion tracking for the optimization of radiation therapy. During the respiration, Phase 5 in Fig. 1 is relatively stable due to its very small volume change. We construct a surface model of the lung as well as the tumor directly from the CT data at Phase 5, and define it as the reference.

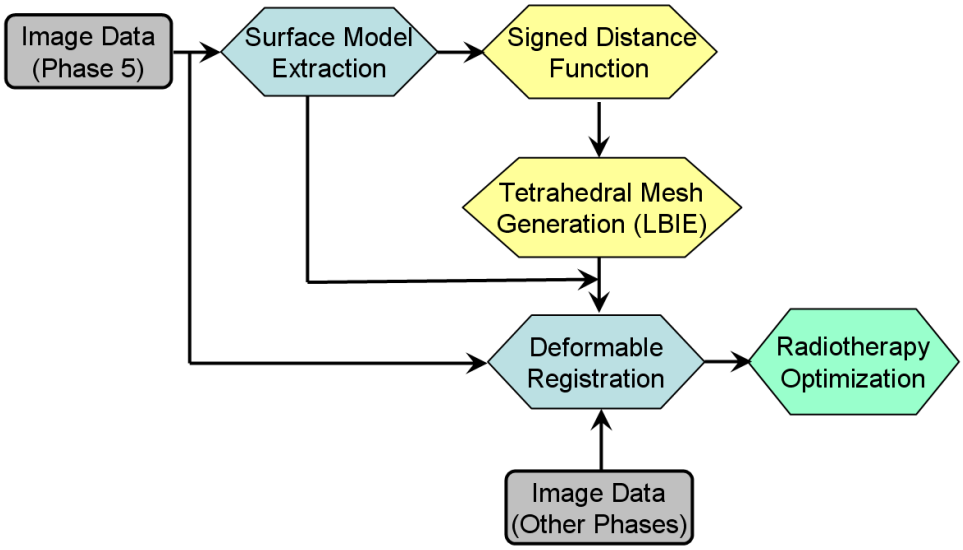

Figure 2: Pipeline of dynamic lung modeling and tumor tracking for radiotherapy optimization.

The triangular surface mesh of the lung model is generated using our in-house software named LBIE-Mesher (Level-set Boundary Interior and Exterior Mesher) [12]; [13]. Noise may exist in the constructed 3D surface models, therefore geometric flows (or geometric partial differential equations) [14]; [15] are adopted to smooth the surface and improve the aspect ratio of the surface mesh, while preserving surface features. Fig. 3 shows one constructed lung model with tumor. The constructed surface is then converted to volumetric grid data using the signed distance function method, which puts the surface into grids and calculates the shortest distance from each grid point to the surface, and finally assigns different signs to grids inside and outside the boundary. Then the volumetric data will be used as input to generate tetrahedral meshes for the lung-tumor model. Both triangular and

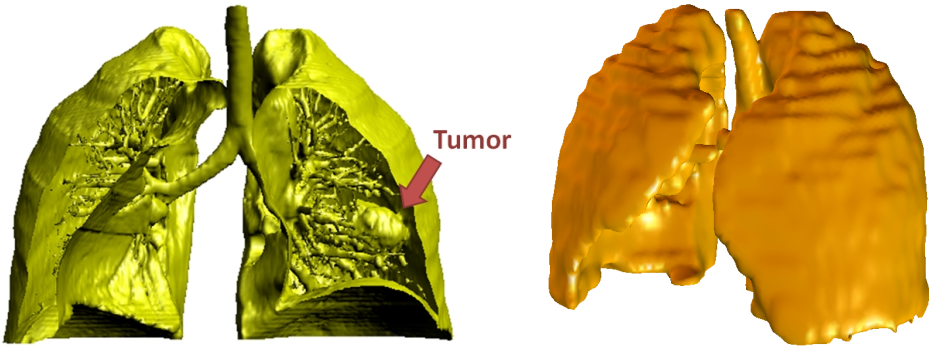

(a) (b)

Figure 3: The extracted surface model of the lung (a) and the triangular mesh after smoothing (b).

tetrahedral meshes will be used in the following dynamic lung modeling and tumor tracking.

3 Deformable Image Registration

CT images are used in radiation dose calculation because Hounsfield units (CT pixel values) are calibrated to the attenuation coefficient of water and therefore the pixel values are well defined. CT images directly reflect tissue density, therefore we choose an intensity-based algorithm for radiotherapy application [16]. Our algorithm is based on an optical flow method, also known as the "demons" algorithm [8], together with a geometric smoothing technique.

3.1 Optical Flow

Given one static image S and one moving image M, the "demons" algorithm evaluates the demons force using the gradient of the intensity field from S to match these two images. Usually, the optical flow formula is applied to calculate one passive force $\vec{f}_s$ at grid point on a greyscale image,

$$\vec{f}_s = \frac{(m-s)\vec{\nabla}s}{|\vec{\nabla}s|^2 + (s-m)^2}, \tag{1}$$

where $\vec{\nabla}s$ is the gradient on the static image. This algorithm may not be efficient especially when image varies little among neighboring grid points in one local region. Based on Newton's third law of motion, an active force f_m was introduced

to speed up the rate of convergence by making use of information from both static and moving images,

$$\vec{f}_m = -\frac{(s-m)\vec{\nabla}m}{|\vec{\nabla}m|^2+(s-m)^2}. \tag{2}$$

The term "passive" force denotes the contribution to the force from the static image. Similarly, the term "active" force denotes the influence from the moving image, in which the deformation is iteratively calculated to match with the moving image and it is active to track the corresponding point on the moving image. Combining f_s and f_m, the total force at a specific grid point can be calculated as

$$\vec{f} = \vec{f}_s + \vec{f}_m = (m-s)\left(\frac{\vec{\nabla}s}{|\vec{\nabla}s|^2+(s-m)^2} + \frac{\vec{\nabla}m}{|\vec{\nabla}m|^2+(s-m)^2}\right). \tag{3}$$

Eqn (3) is suitable for 3D image analysis with a complete grid of demons, and can deal with large deformation between two images. However, it may not be able to capture the boundary precisely. Therefore, we introduce "demons 2" to improve the performance along the boundary. For each contour point P in S, the "passive" and "active" forces are obtained using

$$\vec{f}_s' = K(m)\vec{n}_s \quad and \quad \vec{f}_m' = K(m)\vec{n}_m, \tag{4}$$

where $\vec{n}_s$ is the oriented normal of the contour point in S, and $\vec{n}_m$ is the oriented normal of the contour point in M (both from inside to outside). $K(m)$ is the demon function, see Fig. 4. In the figure, $s_{in} = s(P-2\vec{n}_s)$, $s_{out} = s(P+2\vec{n}_s)$, and P is the position vector of this contour point. Combining both "passive" and "active" forces, we can obtain the total demon force,

$$\vec{f}' = K(m)(\vec{n}_s + \vec{n}_m). \tag{5}$$

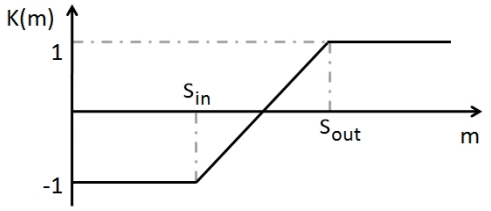

Figure 4: The $K(m)$ function in "demons 2".

3.2 Geometric Smoothing

To obtain smooth geometry after registration, we also include a geometric smoothing technique into our algorithm besides the Gaussian filter on the image domain. Here, we minimize an energy functional

$$\mathscr{E}(\mathbf{x}) = \int_{\Omega} (g(\mathbf{x}(u,v,w)) - 1)^2 du dv dw, \tag{6}$$

where $\Omega = [0,1]^3$, $\mathbf{x}(u,v,w)$ is the position vector of one grid point, and

$$g(\mathbf{x}) = g_{11}g_{22}g_{33} + 2g_{12}g_{23}g_{13} - (g_{13}^2 g_{22} + g_{23}^2 g_{11} + g_{12}^2 g_{33}) \tag{7}$$

with $g_{11} = \mathbf{x}_u^T \mathbf{x}_u$, $g_{12} = \mathbf{x}_u^T \mathbf{x}_v$, $g_{13} = \mathbf{x}_u^T \mathbf{x}_w$, $g_{22} = \mathbf{x}_v^T \mathbf{x}_v$, $g_{23} = \mathbf{x}_v^T \mathbf{x}_w$, and $g_{33} = \mathbf{x}_w^T \mathbf{x}_w$. For the existence of the solution of Eqn (6), see [17]. Here, we construct an L^2-gradient flow by minimizing the energy functional $\mathscr{E}(x)$,

$$\bar{\mathbf{x}}(u,v,w,\varepsilon) = \mathbf{x} + \varepsilon \Phi(u,v,w), \tag{8}$$

where $u,v,w \in \Omega$ and $\Phi \in C_0^1(\Omega)^2$. Then, we have

$$\delta(\mathscr{E}(x), \Phi) = \frac{d}{d\varepsilon} \mathscr{E}(\bar{\mathbf{x}}(\cdot,\varepsilon))|_{\varepsilon=0} = 2\int_{\Omega} (g(\mathbf{x}(u,v,w)) - 1)\delta(g) d\Omega. \tag{9}$$

Hence, the equation becomes

$$\delta(\mathscr{E}(x), \Phi) = 2\int_{\Omega} (\Phi_u^T \alpha + \Phi_v^T \beta + \Phi_w^T \gamma) du dv dw. \tag{10}$$

After applying Green's theorem, we have

$$\delta(\mathscr{E}(x), \Phi) = -2\int_{\Omega} \Phi^T (\alpha_u + \beta_v + \gamma_w) du dv dw + const, \tag{11}$$

where $\alpha_u = 2 * (\frac{\partial g(x)}{\partial u}(\mathbf{x}_u g_{22}g_{33} + \mathbf{x}_v g_{23}g_{13} + \mathbf{x}_w g_{12}g_{23} - \mathbf{x}_w g_{13}g_{22} - \mathbf{x}_v g_{12}g_{33} - \mathbf{x}_u g_{23}^2) +$
$(g(x)-1)(\mathbf{x}_{uu}g_{22}g_{33} + \mathbf{x}_u \frac{\partial g_{22}}{\partial u} g_{33} + \mathbf{x}_u \frac{\partial g_{33}}{\partial u} g_{22} + \mathbf{x}_{vu} g_{23}g_{13} + \mathbf{x}_v \frac{\partial g_{23}}{\partial u} g_{13} + \mathbf{x}_v \frac{\partial g_{13}}{\partial u} g_{23} +$
$\mathbf{x}_{wu} g_{12}g_{23} - \mathbf{x}_w \frac{\partial g_{12}}{\partial u} g_{23} + \mathbf{x}_w \frac{\partial g_{23}}{\partial u} g_{12} - \mathbf{x}_{wu} g_{13}g_{22} - \mathbf{x}_w \frac{\partial g_{13}}{\partial u} g_{22} - \mathbf{x}_w \frac{\partial g_{22}}{\partial u} g_{13} - \mathbf{x}_{vu} g_{12}g_{33} -$
$\mathbf{x}_v \frac{\partial g_{12}}{\partial u} g_{33} - \mathbf{x}_v \frac{\partial g_{33}}{\partial u} g_{12} - \mathbf{x}_{uu} g_{23}^2 - 2\mathbf{x}_u \frac{\partial g_{23}}{\partial u} g_{23}))$;

$\beta_v = 2 * (\frac{\partial g(x)}{\partial v}(\mathbf{x}_v g_{11}g_{33} + \mathbf{x}_u g_{23}g_{13} + \mathbf{x}_w g_{12}g_{13} - \mathbf{x}_u g_{12}g_{33} - \mathbf{x}_w g_{23}g_{11} - \mathbf{x}_v g_{13}^2) +$
$(g(x)-1)(\mathbf{x}_{vv}g_{11}g_{33} + \mathbf{x}_v \frac{\partial g_{11}}{\partial v} g_{33} + \mathbf{x}_v \frac{\partial g_{33}}{\partial v} g_{11} + \mathbf{x}_{uv} g_{23}g_{13} + \mathbf{x}_u \frac{\partial g_{23}}{\partial v} g_{13} + \mathbf{x}_u \frac{\partial g_{13}}{\partial v} g_{23} +$
$\mathbf{x}_{wv} g_{12}g_{13} + \mathbf{x}_w \frac{\partial g_{12}}{\partial v} g_{13} + \mathbf{x}_w \frac{\partial g_{13}}{\partial v} g_{12} - \mathbf{x}_{uv} g_{12}g_{33} - \mathbf{x}_u \frac{\partial g_{12}}{\partial v} g_{33} - \mathbf{x}_u \frac{\partial g_{33}}{\partial v} g_{12} - \mathbf{x}_{wv} g_{23}g_{11} -$
$\mathbf{x}_w \frac{\partial g_{23}}{\partial v} g_{11} - \mathbf{x}_v \frac{\partial g_{11}}{\partial v} g_{23} - \mathbf{x}_{vv} g_{13}^2 - 2\mathbf{x}_v \frac{\partial g_{13}}{\partial v} g_{13}))$; and

$\gamma_w = 2 * (\frac{\partial g(x)}{\partial w}(\mathbf{x}_w g_{11} g_{22} + \mathbf{x}_v g_{12} g_{13} + \mathbf{x}_u g_{12} g_{23} - \mathbf{x}_u g_{13} g_{22} - \mathbf{x}_v g_{23} g_{11} - \mathbf{x}_w g_{12}^2) + (g(x)-1)(\mathbf{x}_{ww} g_{11} g_{22} + \mathbf{x}_w \frac{\partial g_{11}}{\partial w} g_{22} + \mathbf{x}_w \frac{\partial g_{22}}{\partial w} g_{11} + \mathbf{x}_{vw} g_{12} g_{23} + \mathbf{x}_v \frac{\partial g_{12}}{\partial w} g_{23} + \mathbf{x}_v \frac{\partial g_{23}}{\partial w} g_{12} + \mathbf{x}_{uw} g_{12} g_{23} + \mathbf{x}_u \frac{\partial g_{12}}{\partial w} g_{23} + \mathbf{x}_u \frac{\partial g_{23}}{\partial w} g_{12} - \mathbf{x}_{uw} g_{13} g_{22} - \mathbf{x}_u \frac{\partial g_{13}}{\partial w} g_{22} - \mathbf{x}_u \frac{\partial g_{22}}{\partial w} g_{13} - \mathbf{x}_{vw} g_{23} g_{11} - \mathbf{x}_v \frac{\partial g_{23}}{\partial w} g_{11} - \mathbf{x}_v \frac{\partial g_{11}}{\partial w} g_{23} - \mathbf{x}_{ww} g_{12}^2 - 2\mathbf{x}_v \frac{\partial g_{12}}{\partial w} g_{12}))$.

We define a term $G = -2\lambda(\alpha_u + \beta_v + \gamma_w)$ (λ is an input parameter), and merge it with Eqns (3) and (5). Then, we obtain

$$\vec{f} = \vec{f}_s + \vec{f}_m + \vec{f}'_s + \vec{f}'_m - G. \tag{12}$$

To apply the displacement field from image grid points to the mesh model, a trilinear interpolation on 3D regular grids is used to calculate the corresponding displacement of the mesh model. All the information required is the intensity value of each grid point on the static and moving images. As shown in Fig. 5, Eqn (12) is calculated iteratively. In each iteration, the regularization of the deformation field and geometric smoothing follow this optical flow calculation, using a Gaussian filter with a variance of σ^2 (here we choose σ =1.0) and the G term in Eqn (12). The regularization plays an essential role as a smoothing operation to remove noise and preserve the geometric continuity, when this algorithm calculates displacement merely using the local information. After each iteration a stopping criterion is required. For each mesh vertex, if the maximum displacement difference is smaller than a given threshold as which we set 0.01, which is roughly 10% of the minimum span among X, Y and Z coordinates, the program stops.

4 Testing Results and Discussion

We have applied our algorithm to 2D lung images. For example, we took the same transverse cross section (slice 48) from the lung images at Phase 5 and Phase 9. In Fig. 6, (a) shows the contour curve overlaid with the static image at Phase 5. In (b), the green curve denotes the contour curve in (a) overlaid with the moving image at Phase 9, the red curve denotes the deformed contour using demons 1&2, and the blue curve denotes the deformed contour using demons 1&2 and with G term influence. The deformed grids are shown in (c) and (d). It is obvious that the deformed isocontour matches with the moving image very well, and with G terms the deformed grids are much smoother. As shown in Fig. 7, this can be verified again using the same coronal cross section (slice 250) at Phases 5 and 9, which shows more obvious movement of the tumor.

In addition, we applied our algorithm to tetrahedral lung mesh and calculated the volume at each time phase. We generated the tetrahedral mesh directly from Phase

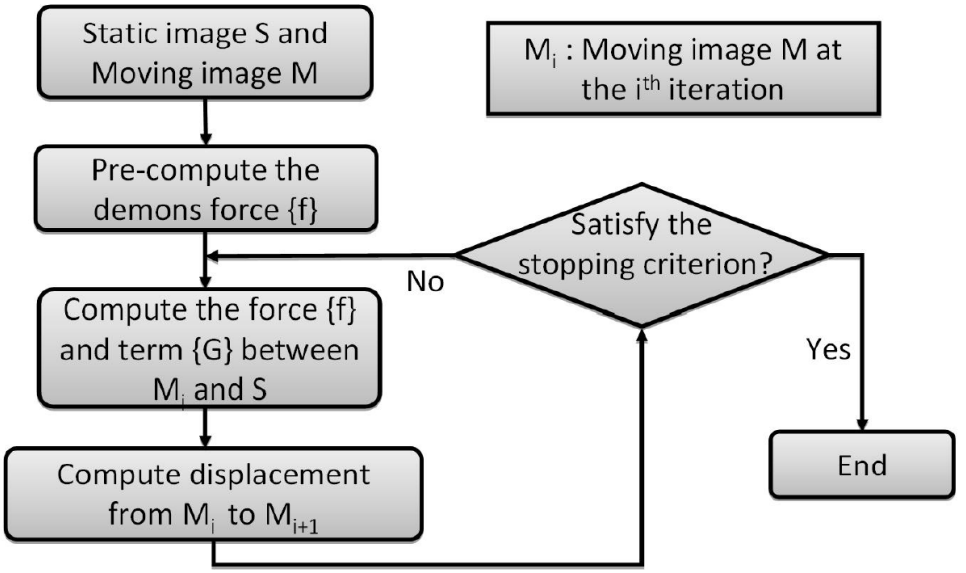

Figure 5: The iterative scheme for the optical flow and geometric smoothing.

5 image data utilizing our meshing tool LBIE-Mesher. In Fig. 8, the blue line denotes the registration result using our algorithm, which always takes Phase 5 as the reference phase to generate the targeted tetrahedral meshes. The green line denotes the registration results, which takes the adjacent phase mesh (obtained from registration) as the reference to generate the targeted tetrahedral mesh in two different directions, one is Phase 5-4-3-$\cdots$-7-6-5 and the other one is Phase 5-6-7-$\cdots$-3-4-5. After finishing both computations, we took the average of these two sets of results. From the results, we can observe that the gradual registration yields a better match with Fig. 1, with the volume change reaching the maximum at Phase 0 through the ten phases of one cycle.

Furthermore, we applied our algorithm to the triangle surface mesh and calculated the maximum displacement of the left lung, the right lung and the tumor during the breath, see Fig. 9. The green line denotes the maximum displacement of the left lung, where the tumor was. The red and blue lines denote the maximum displacement of the right lung and the tumor, respectively. Ideally, both the left and right lungs should deform roughly in the same displacement range. From this figure, it is obvious that the left lung deforms irregularly (at Phase 3) and the tumor can move as large as $1cm$. This is because the lung tumor is one kind of abnormal mass consisting of non-active lung tissues, it has lost the functionality of the regular lung cell during inspiration and expiration. The moving trajectory of the tumor can be used

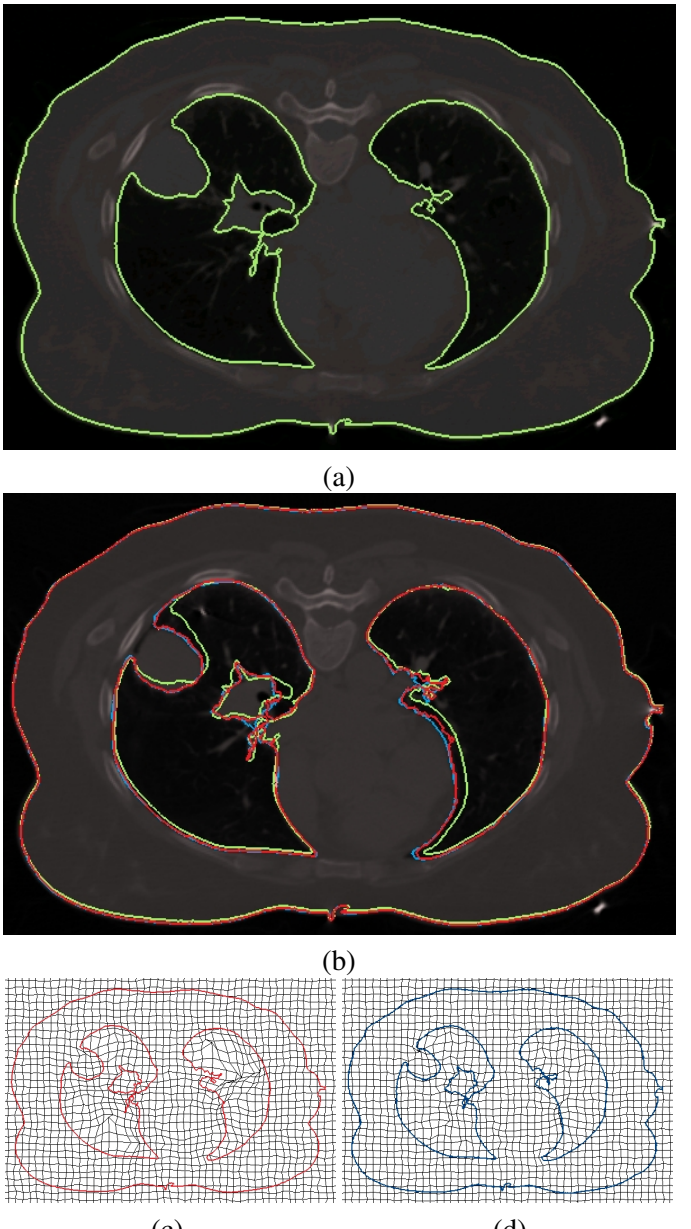

(a)

(b)

(c) (d)

Figure 6: Registration results of 2D lung images (transverse cross sections) at Phases 5 and 9. (a) The contour curve overlaid with the static image at Phase 5; (b) the green curve denotes the contour in (a) overlaid with the moving image at Phase 9, the red curve denotes the deformed contour without G term influence, and the blue one denotes the deformed contour with G term influence; (c) the deformed grids without G term influence; and (d) the deformed grids with G term influence.

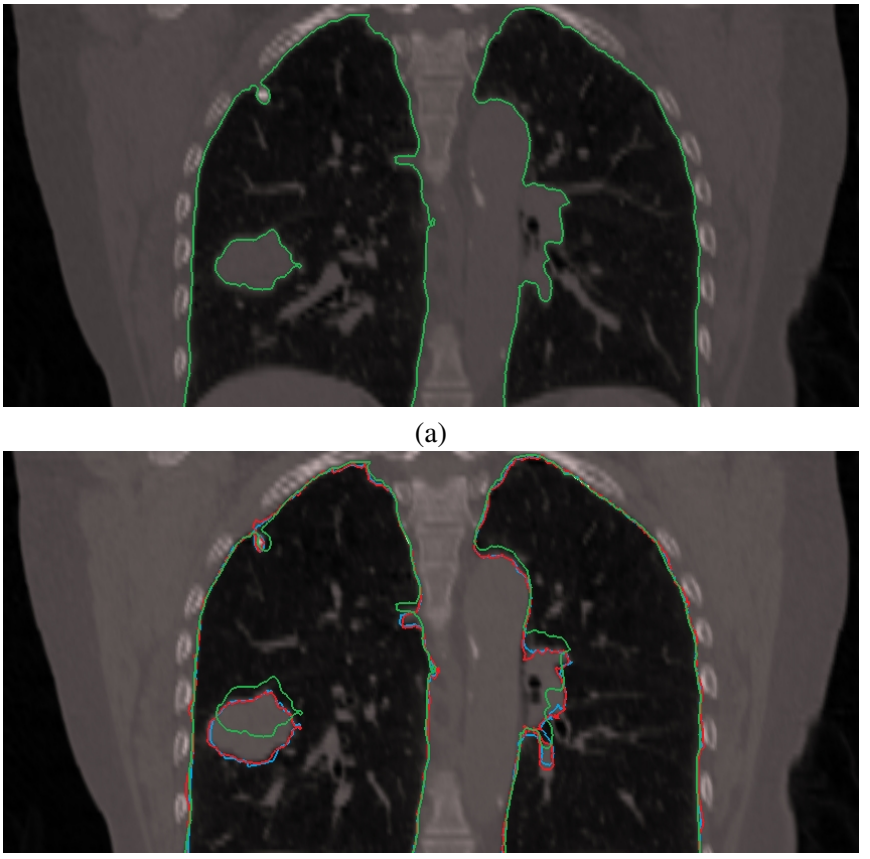

(a)

(b)

Figure 7: Registration results of 2D lung images (coronal cross sections) at Phases 5 and 9. (a) The contour curve overlaid with the static image at Phase 5; and (b) the green curve denotes the contour in (a) overlaid with the moving image at Phase 9, the red curve denotes the deformed contour without G term influence, and the blue one denotes the deformed contour with G term influence.

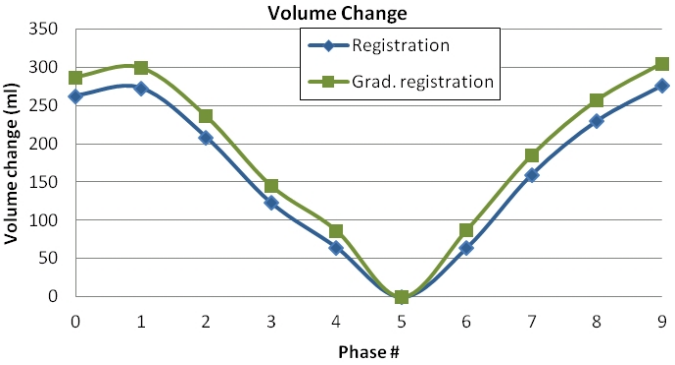

Figure 8: The volume change using various methods.

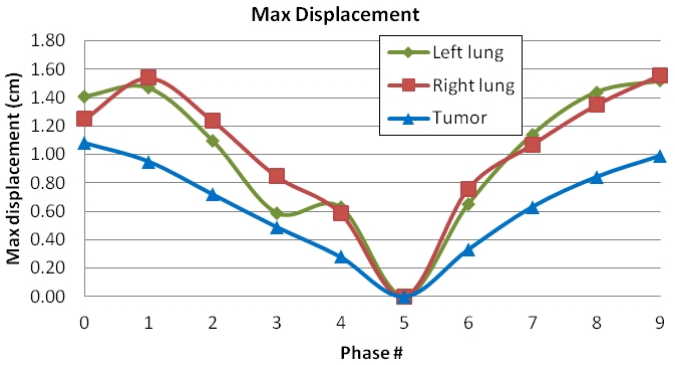

Figure 9: The maximum displacement of the left lung, the right lung and the tumor.

to control the movement of the radiation probes, and thus to optimize the radiation therapy for lung cancer treatment planning.

Discussion. Compared to the standard tidal lung volume in Fig. 1, the maximum volume change in Fig. 8 is much smaller. This is reasonable because each patient is different. From Fig. 9, we can observe that during the respiration, the tumor movement can be large, even reach 1-2cm. In addition, the physical condition of this patient is not good due to the large size tumor, which contributes to the shortness of breath. Since we do not know much about the health situation of that patient, we merely deduce that the lung tumor leads to the reduced lung displacement, especially for the left lung with the tumor.

5 Conclusions

We have developed an effective deformable image registration technique using the optical flow method together with geometric smoothing, which was validated using a set of 4D CT images of the lung. However, we only tested our technique on limited samples. As part of our future work, we will test more datasets and compare with other state-of-art techniques. There are several potential developments which could improve this technique, such as multi-resolution registration. To effectively register two images from large structure features to fine details, in the future we will investigate new techniques supporting multi-resolution alignment. In addition, we will study how to identify the detailed level for each grid point based on the intensity gradient information. In this way, we can skip quite a lot grid points whose neighboring points vary little, and thus to improve the effectiveness of this algorithm.

Acknowledgement: A preliminary version of this paper has been accepted by the CompIMAGE (Computational Modeling of Objects Presented in Images: Fundamentals, Methods and Applications) 2012 conference [18]. This research was supported in part by a research grant from the Winters Foundation.

Reference

[1] R. Siegel, E. Ward, O. Brawley, and A. Jemal. Cancer statistics, 2011. *CA: A Cancer Journal for Clinicians*, 61(4):212–236, 2011.

[2] Barbara Zitová and Jan Flusser. Image registration methods: a survey. *Image and Vision Computing*, 21:977–1000, 2003.

[3] R. Bajcsy and S. Kovacic. Multiresolution elastic matching. *Computer Vision, Graphics, and Image Processing*, 46(1):1–21, 1989.

[4] C. Davatzikos, J. Prince, and R. Bryan. Image registration based on boundary mapping. *IEEE Transactions on Medical Imaging*, 15(1):112–115, 1996.

[5] S. Osher and R. Fedkiw. *Level set methods and dynamic implicit surfaces*. Springer-Verlag, 2003.

[6] M. Moelich and T. Chan. Joint segmentation and registration using logic models. In *UCLA CAM Report 03-06*, February 2003.

[7] Mark Droske and Wolfgang Ring. A mumford–shah level-set approach for geometric image registration. *SIAM Journal on Applied Mathematics*, 66(6): 1–19, 2006.

[8] J. P. Thirion. Image matching as a diffusion process: an analogy with Maxwell's demons. *Medical Image Analysis*, 2(3):243–260, 1998.

[9] P. R. Andresen and M. Nielsen. Non-rigid registration by geometry-constrained diffusion. *Medical Image Analysis*, 5(2):81–88, 2001.

[10] Berthold K. P. Horn and Brian G. Schunck. Determining optical flow. *Artifical Intelligence*, 17:185–203, 1981.

[11] J. L Barron, D. J Fleet, and S. S Beauchemin. Systems and experiment: performance of optical flow techniques. *International Journal of Computer Vision*, 12:43–77, 1994.

[12] Y. Zhang, C. Bajaj, and B.-S. Sohn. 3D finite element meshing from imaging data. *Computer Methods in Applied Mechanics and Engineering*, 194:5083–5106, 2005.

[13] Y. Zhang and C. Bajaj. Adaptive and quality quadrilateral/hexahedral meshing from volumetric data. *Computer Methods in Applied Mechanics and Engineering*, 195(9-12):942–960, 2006.

[14] Y. Zhang, G. Xu, and C. Bajaj. Quality meshing of implicit solvation models of biomolecular structures. *Computer Aided Geometric Design*, 23(6):510–530, 2006.

[15] Y. Zhang, C. Bajaj, and G. Xu. Surface smoothing and quality improvement of quadrilateral/hexahedral meshes with geometric flow. *Communications in Numerical Methods in Engineering*, 25(1):1–18, 2009.

[16] H. Wang, L. Dong, J. O'Daniel, R. Mohan, A. Garden, K. Ang, D. Kuban, M. Bonnen, J. Chang, and R. Cheung. Validation of an accelerated demons algorithm for deformable image registration in radiation therapy. *Physics in Medicine and Biology*, 50(12):2887–2905, 2005.

[17] G. Xu. Geometric partial differential equation methods in computational geometry. *Scientific Publishing Press*, pages 215–220, 2008.

[18] Y. Zhang, Y. Jing, X. Liang, G. Xu, and L. Dong. Dynamic lung modeling and tumor tracking using deformable image registration and geometric smoothing. In *CompImage (Computational Modeling of Objects Presented in Images: Fundamentals, Methods and Applications), accepted*, 2012.